PERMEABILITY OF SHORT FIBER REINFORCED POWDER METALLURGY MATERIAL AND ITS APPLICATION IN POROUS MOLD

Bibo Yao,[1] **Zhaoyao Zhou,**[1,2] **Liuyang Duan,**[1]
and Zhiyu Xiao[1]

Permeability is one of the key properties for understanding the fluid flow and pressure drop in porous metal. In this study, a novel 304 stainless steel fiber reinforced powder metallurgy (P/M) material is produced. Stainless steel powders and short fibers are alternately laid in layers according to mass fraction and then sintered to produce the porous material. Air and water permeability tests are conducted to characterize the permeability of the material. The powder mesh, porosity, and pore size are varied to investigate the effect of permeability. Porous molds made of the material are designed to perform paperboard molding and plastic-injection experiments. The results demonstrate that the relationship between pressure drop per unit length and flow velocity is a parabola, where air or water flows through the P/M material. The permeability coefficient decreases with increasing powder mesh. Compared to water going through the material, the permeability coefficient is higher and the inertial loss is more significant in case of air. The pore size has greater effect on the permeability, than porosity. The perfect appearance of the paperboard presents a good permeability of the P/M material, showing the promising application in molding.

Keywords: powder metallurgy material, permeability, inertial loss, pore size, porosity.

INTRODUCTION

Porous materials with special structure and functional properties have attracted attention for their outstanding thermal, acoustic, electrical, and mechanical properties [1, 2]. They are now applied in filtration and separation [3], diffusion of fluid and gas [4], energy absorption [5], heat transfer [6], etc. However, porous materials are not widely used in mold industry for their property deficiency. The main application in mold industry is the injection mold. Plastic injection molding is an important method to produce high polymers, ensuring stable structural shape of products, decreasing production cycle and costs [7]. It plays a dominant role in plastic manufacturing as one of the main plastic deforming methods [8, 9]. In mold filling, the venting system is usually used to exhaust residual gas, however, it complicates mold design [10]. When inadequate venting, the defects, such as short shot, cavitation, and flow marks, can occur. The conventional venting methods, including parting surface, exhaust holes and slots, cannot reach the expectation when mold structure is complicate or chamber is small.

[1]School of Mechanical and Automotive Engineering, South China University of Technology, Guangzhou, China.

[2]To whom correspondence should be addressed; e-mail: zhyzhou@scut.edu.cn.

Cooling system plays an important role in injection molding, while unreasonable cooling system causes the warping deformation of the plastic products. The demolding of plastic products affects their quality and appearance. Some large or sophisticated parts cannot be demolded successfully unless venting system is added. The studies [11, 12] have reported that the release of micro structure parts was realized by using the air stripping method. The aerodynamic stripping method needs micro holes opened around the cavity, however, the air holes are easily blocked. It should be noted that the venting system is difficult to be integrated into the mold in some cases. The application of porous materials in molds is a promising method of solving the problem.

The investigations on porous materials mainly focus on their forming methods, properties, and application [13–15]. The invention of permeable steel makes it promising to solve the gas exhausting problem of injection molding. It is critical to understand the associated pressure drop behavior in porous materials as it directly affects the filtration effectiveness and the required pumping power in practical applications [16]. At present, the porous material is gradually used in gas exhausting, cooling, demolding, and molding. Permeable steel with porosity of 17% was designed and produced, and the plastic-injection experiment was conducted to investigate its permeability [10]. Sintered porous metal was used in the mold in the injection molding of a thermometer shell, and solved the gas exhausting problem of thin-walled billet properly [17]. Andres [18] invented back pressure and cooling systems by using porous materials in automotive interior decoration in molding. The cooling time and the molding cycle were shortened. The density of parts was improved, and the warpage defect was reduced.

The permeability of porous materials has its unique advantages in molding. Though porous metals are widely used in injection molding, we still have no detailed investigation and only few reports have been seen about the application in paperboard mold industry. It is necessary to investigate the permeable properties of porous metal materials. Porous metal materials are usually produced by the powder metallurgy (P/M) technique. Nevertheless, sintered powder materials are too brittle to withstand heavy loads and limited in engineering for their insufficient mechanical properties. In this study, the fiber-reinforced P/M material produced by using solid-state sintering of stainless steel powders and short fibers, as the method in our early investigation [19], revealed good mechanical properties. Then the water and air permeability were experimentally investigated. Eventually, the paperboard molding experiment was conducted to study the application of porous materials in molding industry.

EXPERIMENTAL PROCEDURE

Processing Procedures of P/M Material. The P/M material samples were produced according to the procedures described in [19].

First, short stainless steel fibers (100 and 160 μm dia; 5–8 mm long) were produced by cutting 304 steel wires with a rotary multi-cutter tool. Next, stainless steel powders and fibers were put into a specially assembled mold by the method of alternately laying powders and fibers in layers according to the mass fraction, and then compacted under 75 MPa (Fig. 1). The material without compaction pressure was produced by laying powders and fibers using the same method. Upon completion, compacts were produced. To prevent oxygenation, the sintering was carried out in a WHS-20 (Zhongshan Kaixuan vacuum technology and Engineering Co. Ltd., China) pressurized air cooling vacuum sintering furnace with vacuum degree about $5 \cdot 10^{-2}$ Pa. Stage heating method was used to optimize the heating rate. When the temperature was below 800°C, the heating rate was kept at $10°C \cdot h^{-1}$. After reaching 800°C, the temperature was kept for ~60 min. To complete the process, the heating rate was reduced to $5°C \cdot h^{-1}$ until 1350°C. Finally, the temperature was kept at 1350°C for ~60 min and then the samples were cooled in the furnace to room temperature. Upon completion of the process, sample 1 (powder size 35 mesh; 160 μm dia. fiber; mass fraction 6 wt.%; compacting pressure 0 MPa), sample 2 (powder size 100 mesh; 100 μm dia. fiber; mass fraction 6 wt.%; compacting pressure 75 MPa), and sample 3 (powder size 200 mesh; 100 μm dia. fiber; mass fraction 6 wt.%; compacting pressure 0 MPa) were produced.

The porosity of porous material was determined by the quality-volume method using the equation [15]:

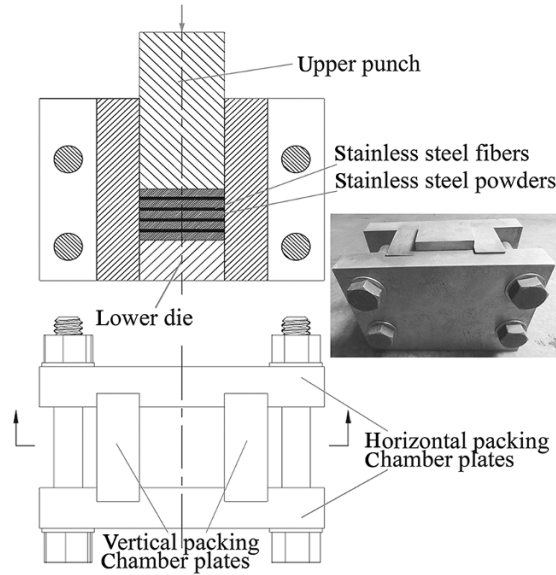$$\varepsilon = \left(1 - \frac{m}{\rho_s V}\right) \cdot 100\% , \tag{1}$$

Fig. 1. Mold-pressing equipment of P/M materials

where ρ is the density of the P/M material (g/cm^{-3}); ρ_s is the density of 304 stainless steel (g/cm^{-3}); m is the mass of the P/M material (g); V is the volume of the P/M material (cm^3). The porosities of the samples 1, 2, and 3 were 71.10, 47.20, and 52.00%, respectively.

The microscopic morphology of P/M material was observed using a S-3700N scanning electron microscope (Tokyo, Japan). The method of excluding gas and liquid was employed for measuring the pore size using a PSDA-20 aperture analyzer (Nanjing Zhongchao environmental protection science and Technology Co., Ltd., China).

Permeability Tests of P/M Material: Theory. The permeability of porous materials is the ability of fluid to pass through porous materials under a certain pressure gradient. It can be evaluated by fluid permeability coefficient and inertia coefficient.

For creeping flow of a fluid through a porous medium, the relationship between the pressure drop and the Darcy velocity (i.e., Darcy equation) can be described by the Darcy equation [20]:

$$\frac{\Delta P}{L} = \frac{\mu}{K} v,$$
(2)

where ΔP is the pressure drop, when fluid flows through porous material; L is the length of the porous metal in the flow direction; μ is the fluid viscosity; K is the viscous permeability coefficient; v is the Darcy velocity of the fluid flow. However, Darcy's law is available only for relatively slow flow velocity, where the permeability-based Reynolds number is small [21]:

$$\mathbf{Re}_K = \frac{\rho \sqrt{K}}{\mu} v < o(1),$$
(3)

where $\mathbf{Re}_K$ is the Reynolds number; ρ is the fluid density at room temperature and pressure; $o(1)$ is the small number.

Three different ways can be used to described $\mathbf{Re}_K$. The first method relates to the permeability, K (Eq. (3)). The second method uses larger flow velocity range by a subjective amount. The third method is based on the average pore diameter and can be expressed as follows [21]:

$$\mathbf{Re}_p = \frac{\rho v D_p}{\mu}.$$
(4)

With increasing flow velocity, the inertial loss becomes more important and must be considered to present the pressure-drop. The Forchheimer regime that modifies Darcy's regime can be used to describe the relationship between the pressure drop and velocity according to the following equation [16, 22–24]:

$$\frac{\Delta P}{L} = \frac{\mu}{K}v + \frac{F\rho v^2}{\sqrt{K}},$$
(5)

where F is the coefficient that accounts for inertia/form drag coefficient. Sometimes F is referred to as the Forchheimer coefficient or inertia coefficient. This coefficient represents the blockage of the internal structure to the flow. Both K and F are strongly dependent on the structure of the porous medium.

The permeability K and the inertia coefficient C can be calculated by many ways through experiments. One approach proposed by Givler and Altobelli et al. [25] modified Eq. (5) to bring it into linear form and then extrapolated to determine the coefficients, however, this method cannot calculate the coefficients accurately due to the extrapolation. Therefore, more direct and accurate approach is put forward by Antohe et al. [26] to fit the pressure-drop versus fluid-speed data points by a least-squares quadratic curve. The form coefficient can be used as an accurate uncertainty analysis. The detail curve-fitting process can be described as follows. Making the following substitutions in Eq. (5):

$$A = \frac{\mu L}{K}$$
(6)

and

$$B = \frac{F\rho L}{\sqrt{K}},$$
(7)

yields the following Eq. (8):

$$\Delta P = Av + Bv^2,$$
(8)

where A and B are solved through the least squares curve fit technique. Once A and B are known, the permeability and inertia coefficient are obtained from Eqs. (6) and (7).

Permeability Tests of P/M Material: Air Permeability Test. Figure 2 shows the schematic of air permeability test system. The porous media in the sample room can be changed to three samples. Compressed air which was produced by air compressor was stored in a constant pressure gas storage tank. Then the water in compressed air was removed, when it flew through drift eliminator in front of the sample room to ensure the gas drying. For a given air flow velocity, the control valve was adjusted and air was allowed to flow into the porous medium until steady state. The air-flow meter was used for recording the air flow velocity. The air entered into the sample room after it went through the flow control valve and air-flow meter. The gas manometers installed at the front and back of the sample room measured the pressure before and after the air flew through the samples. The pressure drop can be calculated by the record data.

Permeability Tests of P/M Material: Water Permeability Test. Figure 3 shows the schematic diagram of water permeability test system. The water stored in a water storage tank began to flow as the suction pump started. For a demanded water flow velocity, the control valve was adjusted and water was allowed to flow into the sample room until steady state. Water flow velocity can be directly read through a digital flowmeter. When water passed the sample room, the pressure in the front and back of the sample was measured by inlet and outlet manometer, respectively.
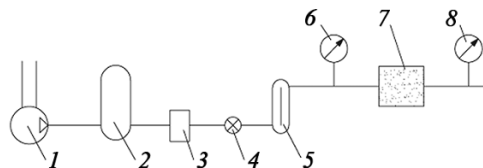

Fig. 2. Schematic diagram of air permeability test system: air compressor (*1*); gas storage tank (*2*); drift eliminator (*3*); flow control valve (*4*); air-flow meter (*5*); inlet gas manometer (*6*); sample room (*7*); outlet gas manometer (*8*)
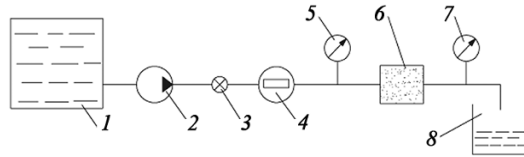
Fig. 3. Schematic diagram of water permeability test system: water storage tank (1); suction pump (2); flow control valve (3); digital flowmeter (4); inlet manometer (5); sample room (6); outlet manometer (7); bucket (8)
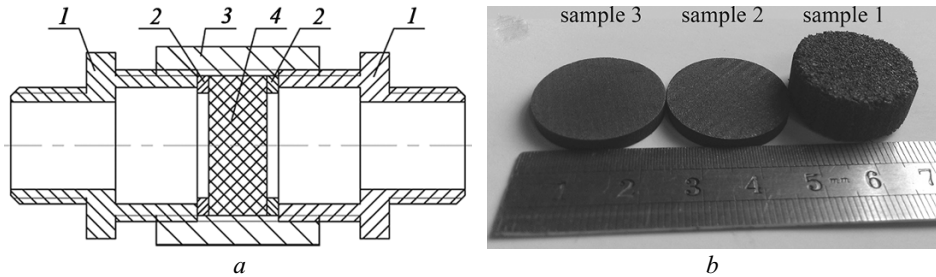

Fig. 4. Schematic diagram of sample room (a) and macroscopic appearance of samples (b): connector (1); seal ring (2); connecting nut (3); and sample (4)

The sample rooms used in air and water permeability tests were the same (Fig. 4). The sample diameter was 24 mm and the thickness of the samples 1, 2, and 3 was 10, 1.8, and 1.8 mm, respectively. The measurements were repeated three times for each sample and the average value was taken as the final result.

Paperboard Molding Experiment. The vacuum suction punch and hot-pressing lower punch were designed and produced using the P/M material to investigate the permeability. The study [19] has investigated the mechanical properties of the materials. The material for producing the vacuum suction punch needed good water permeability but not high strength and, therefore, sample 1 was selected to make the mold. The hot-pressing lower punch needed enough strength to withstand the pressure to get smooth surface after hot pressing and, therefore, sample 3 was chosen to make it. Transferring mold and hot-pressing upper punch were produced of 6061 aluminum alloy. Figures 5 and 6 show the schematic diagrams of cold and hot-pressing mold, respectively.

The process of this experiment could be described as follows. First, paperboards were smashed into paste, and then waterproof anti-oil chemical reagent and water were added to obtain dilute paste. Subsequently, dilute fiber suspension was poured into slurry tank on the vacuum suction punch and pumped through the punch. Thus, a wet billet was formed on the vacuum suction punch. Afterwards, the transferring mold moved down and compounded to extrude the wet billet for water draining. Upon completion of the process, the wet billet was transferred from the
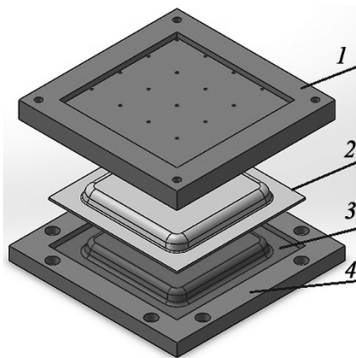

Fig. 5. Setup of cold pressing mold: transferring mold (1); wet billet (2); vacuum suction die (3); fixed frame (4)
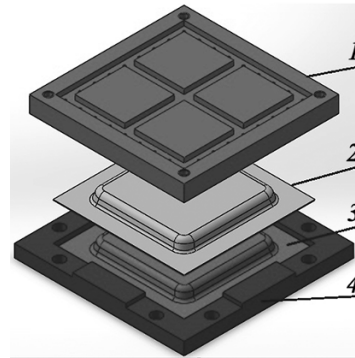

Fig. 6. Setup of hot pressing mold: hot-pressing upper punch (1); product (2); hot-pressing lower punch (3); fixed frame (4)

vacuum suction mold to transferring mold by vacuum suction mold blowing and negative pressure suction of the transferring mold. Then, the transferring mold rose and moved to its station, and the hot-pressing lower punch also moved to its below station. Upon completion of the process, the transferring mold and hot-pressing lower punch were compounded. Meanwhile, the transferring mold blew and hot-pressing lower punch pumped. Thus, the wet billet was transferred to the hot-pressing lower punch. Finally, the hot-pressing lower die was moved to compound with the hot-pressing upper punch for 2 min. Upon completion of the process, the paperboard molding product was produced.

RESULTS AND DISCUSSION

Microstructural Characterization of P/M Material. Before sintering, many contact areas are formed between (among) stainless powders and fibers. With material migration, sintering joints between powders and fibers, among powders and among fibers are produced to enhance the strength of the materials during holding. Figure 7*a* shows the microscopic structure (vertical direction of layers) of sample 3. It is seen that many sintering joints are formed; many microholes are distributed in the metal and the average pore size is 5.28 μm due to the method of excluding gas and liquid. The irregularly shaped powders increase the contact area that promotes the formation of sintering necks as a result of high surface energy. Three types of sintering joints are presented in the metals: powder-to-powder (Fig. 7*b*), fiber-to-fiber (Fig. 7*c*) and powder-to-fiber (Fig. 7*d*) sintering joints. The average pore size of sample 1 is 133.39 μm which is much larger than that of normal P/M material. Samples 1 and 3 have high porosity, 71.10 and 52.00%, respectively. However, the porosity of normal P/M metal ranges from 5% to 15% [27, 28]. Additionally, the fibers in the materials can significantly improve the strength of the P/M materials [19]. Therefore, the P/M material has the potential for better permeability.

Air Permeability of P/M Material. From the data measured, the least-squares quadratic curves of samples 1, 2, and 3 are fitted and the respective uncertainties are calculated according to Eqs. (6)–(8) in Figs. 8*a*, 8*b*, and 8*c*, respectively.

When air density $\rho = 1.205$ kg · m^{-3} and fluid dynamic viscosity $\mu = 1.79 \cdot 10^{-5}$ Pa · sec (101.325 kPa, 20°C), the permeability coefficient K and inertial resistance factor F of three samples are calculated by back-solving the constants A and B from the fitted curves (Eqs. (6) and (7)). Table 1 displays the results. The permeability
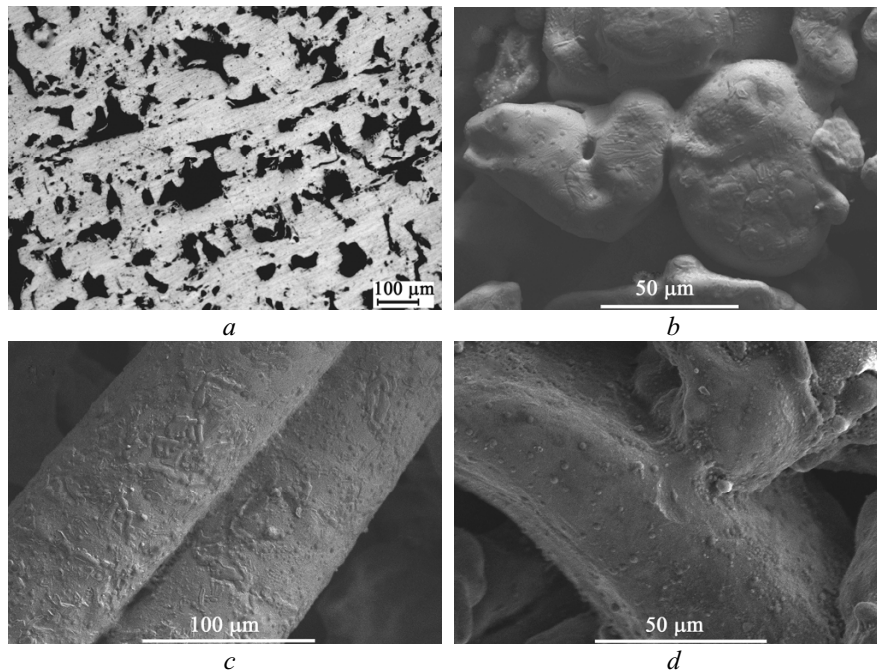

Fig. 7. Microscopic structure of P/M material (*a*); SEM images of sintering joint types in the sample: powder-to-powder (*b*), fiber-to-fiber (*c*), and powder-to-fiber (*d*) sintering joints

TABLE 1. The Permeability Coefficient K and Inertia Coefficient F under Air Working Fluid

Sample number	Porosity, %	Average pore size, μm	Permeability coefficient K, m^2	Inertia coefficient F
1	71.10	133.39	$7.37 \cdot 10^4$	$2.90 \cdot 10^7$
2	47.20	5.26	$5.41 \cdot 10^2$	$2.30 \cdot 10^8$
3	52.00	5.28	$7.54 \cdot 10^{-13}$	10.9

coefficient shows larger value than that of all aluminum foams (4-, 8-, and 16-pore per cm foam samples) in [20], though the foams have lager pore size and porosity. It shows that, compared to the foam, P/M materials have good air permeability. The results reveal the permeability coefficient decrease with increasing powder mesh.

Figure 8*d* compares the pressure-drop experimental data in graphical form for three media. The revision of the data makes clear that the air flows through the P/M materials deviates from Darcy law flow behavior, however fits into Forchheimar law, i.e., the pressure-drop is a quadratic function of the flow velocity. For every sample, the pressure drop per unit length raises with increasing air flow velocity as reported in [20, 29]. The pressure drop per unit length almost keeps the same with increasing flow velocity, when air flows through sample 1 and increases the greatest, when air flows through sample 3. From sample 1 to sample 3, the permeability dramatically reduces from $7.37 \cdot 10^4$ m^2 to $7.54 \cdot 10^{-13}$ m^2. The pressure drop per unit length increases with increasing powder mesh, when the same air flow velocity. It can be explained as follows: compared to other samples, the pore size of sample 1 (30–305.07 μm) is the biggest and the porosity (71.10%) is the largest; interconnected flow channel per volume in sample 1 (the fewest but the biggest) results in simple flow passages, therefore, the flow resistance is the least, when air passes through the flow channel of sample 1; though sample 3 has larger porosity relative to sample 2, sample 3 has more flow passages per volume and the interconnected flow channel is smaller as it has smaller powders, thus, the flow resistance is higher and the pressure drop per unit length is the highest [16]. It is also demonstrated that, compared to porosity, the pore size has greater effect.
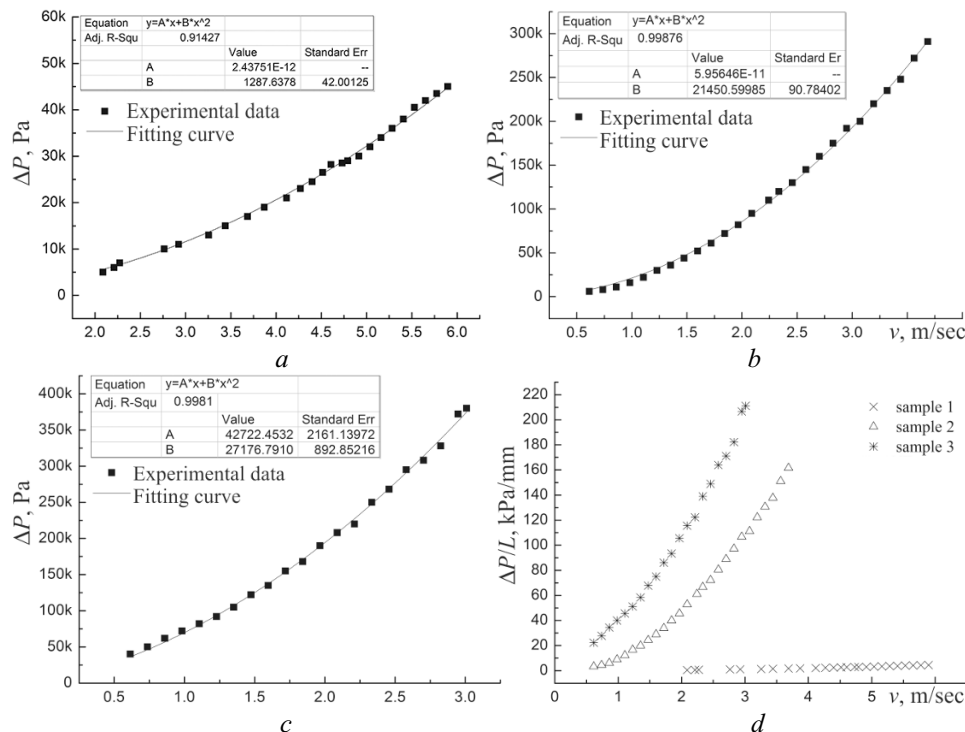

Fig. 8. Fitting curves. Variation of pressure drop with air flow velocity: samples 1 (*a*), 2 (*b*), and 3 (*c*); and pressure drop per unit length with air flow velocity under air conditions (*d*)
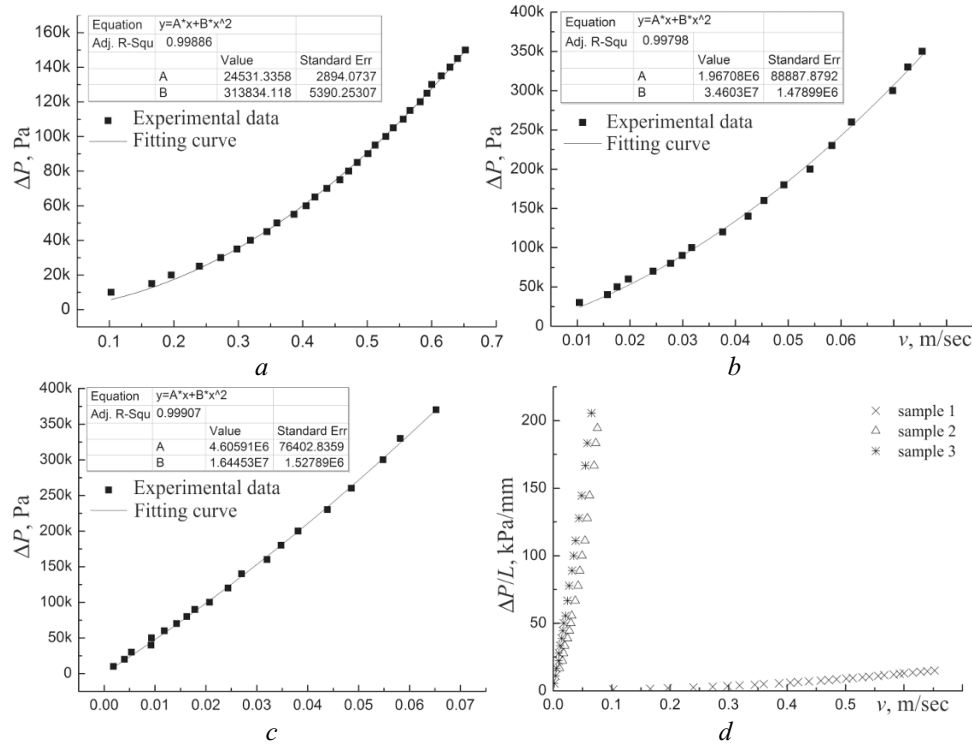
Fig. 9. Fitting curves. Variation of pressure drop with water flow velocity: sample 1 (*a*); sample 2 (*b*), and sample 3 (*c*); and pressure drop per unit length with water flow velocity under water conditions (*d*)

Water Permeability of P/M Material. The relationships between pressure drop and water flow velocity are also fitted with quadratic curves, as well as respective uncertainties are calculated (Fig. 9). The water permeability coefficient K and inertia factor F of three samples are calculated by taking water density ($\rho = 1000$ kg $\cdot$ m^{-3}, 101.325 kPa, 20°C) and fluid dynamic viscosity ($\mu = 1.01 \cdot 10^{-3}$ Pa $\cdot$ sec, 101.325 kPa, 20°C) into Eqs. (6) and (7) (Table 2). From sample 1 to sample 3, the permeability changes from $4.12 \cdot 10^{-10}$ m^2 to $3.94 \cdot 10^{-13}$ m^2. It is interesting to see that sample 2 shows approximately the same permeability as sample 3 does. Since the water fluid dynamic viscosity is high, the average pore size and porosity have little effect, while they have few difference. Additionally, the permeability of sample 1 (i.e., $4.12 \cdot 10^{-10}$ m^2) is nearly lower than that of 92–05 aluminum alloy foam ($8.07 \cdot 10^{-10}$ m^2) but higher than 92–06 aluminum alloy foam. The porosity of 92–05 and 92–06 aluminum alloy foam with 2.3 mm dia. pre-compression pore are 72.2 and 66.9%, respectively [21]. However, the porosity and pore size of sample 1 is 71.1% and 133.39 μm, respectively. Although the aluminum foam has lager pore size and pore channel, It has the similar permeability, which reveals that the P/M material has better permeability. Figure 9*d* compares pressure drop per unit length: flow velocity curve under water conditions. It presents the similar change rule as in case of air permeability: the pressure drop per unit length increases with increasing water flow velocity; it rises as the powder mesh increases at the same water velocity; compared to porosity, the pore size has greater effect on water permeability.

TABLE 2. Permeability Coefficient K and Inertia Coefficient F under Water Working Fluid

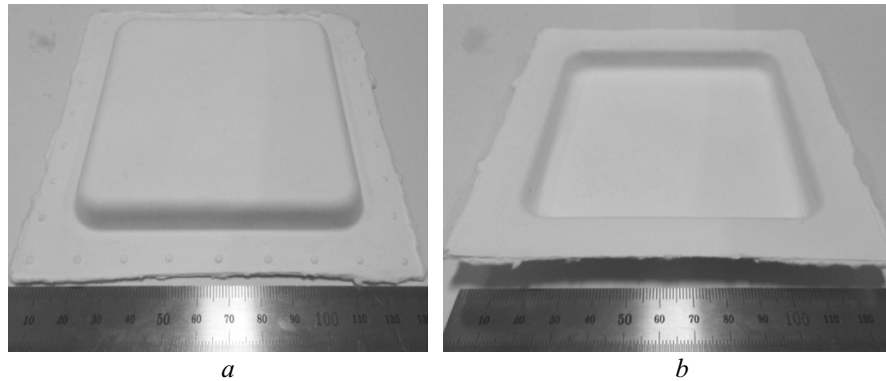| Sample number	Porosity, %	Average pore size, μm	Permeability coefficient K, m^2	Inertia coefficient F
1	71.10	133.39	$4.12 \cdot 10^{-10}$	$6.37 \cdot 10^{-1}$
2	47.20	5.26	$9.28 \cdot 10^{-13}$	18.5
3	52.00	5.28	$3.94 \cdot 10^{-13}$	5.72

Fig. 10. Fiber molding product formed by porous mold: back (*a*); front (*b*)

The comparison of Tables 1 and 2 shows that air permeability coefficient *K* is much greater than that of water for the same sample. This is because the air dynamic viscosity is far lower than that of water and the air viscous resistance is also lower than that of water. It is also noticed that the inertial resistance factor of air is higher than that of water passing through the same sample. Compared to water, the inertial loss is greater, when air flows through the sample.

Paperboard Molding. Figure 10 shows the product without processing after molding. There are convex points left in a front peripheral of the product, where the suction holes on a hot-pressing mold presses the product in the molding. The quality of the front and back are both good. The surfaces are smooth and have no reticulate pattern. The product is easily demolded and the molding is stable. Many interconnected micro holes are distributed in the porous mold, therefore, water can easily get out, while does not need to laterally flow for a long distance. The result demonstrates that the precision molding of fiber molding product can be achieved by applying the P/M material in molding fiber mold.

CONCLUSIONS

Air and water permeability experiments have been conducted to investigate the permeability of the P/M material. The material has been produced by the method of alternately laying stainless steel powders and fibers as the mass ratio and then solid-state sintering.

It has been established that the rule of air and water flowing through the sample has the same changing proprties: (i) parabola relationships exist between pressure drop per unit length and flow velocity, when air or water flows through the P/M material; (ii) pressure drop per unit length increases and permeability coefficient decreases as the powder mesh increases at the same water velocity; (iii) compared to air, the permeability coefficient and inertial resistance are lower when water goes through the same sample; (iv) the inertial loss of air through the sample is more significant than that of water. It has been established that both the porosity and pore size of porous metal affect the permeability, when liquid flows through, however, the pore size has greater effect.

Paperboard molding experiment has been conducted to study the application of the P/M material in mold. Vacuum suction punch and hot-pressing lower punch have been made of P/M material. It has been found out that the production quality is good and the surfaces are smooth without conventional exhaust slots or venting systems for the successful gas and water exhaust from the microholes in a mold. The P/M application in molding industry can be a good choice.

References

1. L. P. Lefebvre, J. Banhart, and D. C. Dunand, "Porous metals and metallic foams: Current status and recent developments," *Adv. Eng. Mater.*, **10**, No. 9, 775–787 (2008).

2. Z. Xi, J. Zhu, H. Tang, et al, "Progress of application researches of porous fiber metals," *Materials*, **4**, No. 4, 816–824 (2011).

3. A.Nabovati, E. W. Llewellin, and A. C. M. Sousa, "A general model for the permeability of fibrous porous media based on fluid flow simulations using the lattice Boltzmann method," *Compos. Pt. A*, **40**, Nos. 6–7, 860–869 (2009).

4. J. K. Kuo and C. K. Chen, "A novel Nylon-6–S316L fiber compound material for injection molded PEM fuel cell bipolar plates," *J. Power Sources*, **162**, No. 1, 207–214 (2006).

5. B. Zhang and T. Chen, "Calculation of sound absorption characteristics of porous sintered fiber metal," *Appl. Acoust.*, **70**, No. 2, 337–346 (2009).

6. A. S. Abduljalil, Z. Yu, and A. J. Jaworski, "Selection and experimental evaluation of low-cost porous materials for regenerator applications in thermoacoustic engines," *Mater. Des.*, **32**, No. 1, 217–228 (2011).

7. C. P. Chen, M. T. Chuang, Y. H. Hsiao, et al., "Simulation and experimental study in determining injection molding process parameters for thin-shell plastic parts via design of experiments analysis," *Expert Syst. Appl.*, **36**, No. 7, 10752–10759 (2009).

8. S. W. Kim and L. S. Turng, "Developments of three-dimensional computer-aided engineering simulation for injection moulding," *Model. Simul. Mater. Sc. Eng.*, **12**, No. 3, S151–S173 (2004).

9. M. C. Yu, W. B. Young, and P. M. Hsu, "Micro-injection molding with the infrared assisted mold heating system," *Mater. Sci. Eng. A*, **460–461**, 288–295 (2007).

10. Z. Zhou, W. Cao, Z. Wu, et al., "Permeable steel and its application in plastic-injection mould," *Chin. J. Mech. Eng.*, **23**, 312–316 (2010).

11. C. Y. Chang, S. Y. Yang, L. S. Huang, et al., "Fabrication of plastic microlens array using gas-assisted micro-hot-embossing with a silicon mold," *Infrared Phys. Technol.*, **48**, No. 2, 163–173 (2006).

12. J. H. Chang and S. Y. Yang, "Gas pressurized hot embossing for transcription of micro-features," *Microsyst. Technol.*, **10**, No. 1, 76–80 (2003).

13. N. Kurgan, "Effect of porosity and density on the mechanical and microstructural properties of sintered 316L stainless steel implant materials," *Mater. Des.*, **55**, 235–241 (2014).

14. A. E. Markaki, V. Gergely, A. Cockburn, et al., "Production of a highly porous material by liquid phase sintering of short ferritic stainless steel fibres and a preliminary study of its mechanical behaviour," *Compos. Sci. Technol.*, **63,** No. 16, 2345–2351 (2003).

15. Y. Tang, W. Zhou, M. Pan, et al., "Porous copper fiber sintered felts: An innovative catalyst support of methanol steam reformer for hydrogen production," *Int. J. Hydrog. Energy*, **33**, No. 12, 2950–2956 (2008).

16. N. Dukhan, Ö. Bagci, and M. Özdemir, "Experimental flow in various porous media and reconciliation of Forchheimer and Ergun relations," *Exp. Therm. Fluid Sci.*, **57**, 425–433 (2014).

17. J. G. Mitchell, *Mold with Porous Cavity Vent*, Patent US 4165062 A, Appl. Jan. 13, 1978, Publ. Aug. 21, 1979.

18. P. E. Andres, *Cooling and Counter-Pressure Method for Producing Plastic Parts by Injection*, Patent US 6855288 B2, Appl. Jan 10, 2001, Publ. Feb. 15, 2005.

19. B. Yao, Z. Zhou, L. Duan, et al., "Compressibility of 304 stainless steel powder metallurgy materials reinforced with 304 short stainless steel fibers," *Materials*, **9**, No. 3, 161 (2016).

20. N. Dukhan and C. A. Minjeur, "A two-permeability approach for assessing flow properties in metal foam," *J. Porous Mater.*, **18**, No. 4, 417–424 (2010).

21. K. Boomsma and D. Poulikakos, "The effects of compression and pore size variations on the liquid flow characteristics in metal foams," *J. Fluids Eng.*, **124**, No. 1, 263–272 (2002).

22. B. Bromley, V. Hessel, A. Renken, et al., "'Sandwich reactor for heterogeneous catalytic processes: N_2O decomposition as a case study," *Chem. Eng. Technol.*, **31**, No. 8, 1162–1169 (2008).

23. P. X. Jiang and X. C. Lu, "Numerical simulation of fluid flow and convection heat transfer in sintered porous plate channels," *Int. J. Heat Mass Transf.*, **49**, Nos. 9–10, 1685–1695 (2006).

24. O. Rahli, L. Tadrist, M. Miscevic, et al., "Fluid flow through randomly packed monodisperse fibers: The Kozeny-Carman parameter analysis," *J. Fluids Eng.*, **119**, No. 1, 188–192 (1997).

25. R. C. Givler and S. A. Altobelli, "A determination of the effective viscosity for the Brinkmann-Forchheimer flow model," *J. Fluid Mech.*, **258**, 355–370 (2006).

26. B. V. Antohe, J. L. Lage, D. C. Price, et al., "Experimental determination of permeability and inertia coefficients of mechanically compressed aluminum porous matrices," *J. Fluids Eng.*, **119**, No. 2, 404–412 (1997).

27. A. Bergmark and L. Alzati, "Fatigue crack path in Cu–Ni–Mo alloyed PM steel," *Fatigue Fract. Eng. Mater. Struct.*, **28**, Nos. 1–2, 229–235 (2005).

28. W. D. Wong-Ángel, L. Téllez-Jurado, J. F. Chávez-Alcalá, et al., "Effect of copper on the mechanical properties of alloys formed by powder metallurgy," *Mater. Des.*, **58**, 12–18 (2014).

29. A. Bhattacharya, V. V. Calmidi, and R. L. Mahajan, "Thermophysical properties of high porosity metal foam," *Int. J. Heat. Mass. Transf.*, **45**, No. 5, 1017–1031 (2002).